Symmetric and asymmetric manipulations of two pulses via dynamically controlled dual-channel optical nonreciprocity

Qian-Qian Bao(鲍倩倩)[1], Xue-Dong Tian(田雪冬)[2*], Yi-Mou Liu(刘一谋)[3]

[1]School of Physics, Liaoning University, Shenyang 110036, China

[2]College of Physics and Technology, Guangxi Normal University and University Engineering Research Center of Advanced Functional Materials and Intelligent Sensing,
Guangxi, Guilin 541004, China

[3]Center for Quantum Sciences and School of Physics, Northeast Normal University, Changchun 130024, China

2026 年 9 月 22 日

Abstract

Optical nonreciprocity provides a firm basis for direction-dependent control of light transport. We propose a scheme to manipulate two counter-propagating light pulses based on dynamically controlled dual-channel optical nonreciprocity originating from the Doppler effect. This scheme is implemented in a four-level tripod-type thermal atomic medium driven by two counter-propagating control fields. Symmetric or asymmetric propagation and storage scenarios for the two probe pulses can be established by adjusting the detunings and intensities of the control fields. In particular, complete separation of the forward and backward transmission windows enables the realization of a frequency-tunable bidirectional optical isolator. Doppler shifts make the tripod system behave as two weakly coupled three-level Λ-type channels associated mainly with the forward and backward probe fields. Our proposal may have potential applications in designing direction-dependent all-optical devices for manipulating multiple optical pulses.

Keywords: Optical nonreciprocity, Doppler effect, electromagnetically induced transparency, optical pulse manipulation

PACS: 42.50.Gy, 42.25.Bs, 32.80.Qk

1. Introduction

Atomic coherence effects, arising from coherent coupling between photons and atoms, have provided us with diverse and effective techniques for manipulating classical or quantum light pulses in the field of

*Corresponding author. E-mail: snowtxd@gxnu.edu.cn

quantum information, such as coherent population transfer [1,2], Autler-Townes splitting [3,4], electromagnetically induced absorption [5] and electromagnetically induced transparency (EIT) [6]. In general, cold or ultra-cold atoms are widely recognized as favorable media for photonic storage and processing, because the Doppler effect (DE) in thermal atoms would lead to the broadening of atomic transition bandwidths and the decay of coherent effects. Therefore, the DE has been commonly regarded as a detrimental effect that should be actively avoided.

However, through an ingenious design, the DE can be used positively in some specific cases. For example, one can obtain a significantly narrower EIT resonance after Doppler averaging [7,8]. Recently, a useful proposal, which employed the DE in an atom-cavity coupling system to achieve nonmagnetic optical nonreciprocal transmission, has garnered considerable attention [9]. It is well known that optical nonreciprocity can be realized by breaking the Lorentz reciprocity theorem and holds great significance in the design of optical devices such as isolators [10–12], circulators [13,14], routers [15,16], and amplifiers [17–19]. In addition to the DE-based scheme, several magnet-free physical mechanisms, more suitable for integration, have also been proposed to achieve optical nonreciprocity. These include dynamical modulation of permittivity [20–23], parity-time symmetry enhanced nonlinearity [24–26], optomechanical interaction [27–33], and chiral quantum optics [34–38]. In fact, the nonreciprocal light propagation based on the DE can be achieved in both cold and hot atoms without cavities. In cold atoms, nonreciprocity arises from the macroscopic DE resulting from moving Bragg lattices [39–42], while in hot atoms, it is rooted in the microscopic DE induced by atomic thermal motion [43–52]. More specifically, the DE-based optical nonreciprocity is obtained with the assistance of various atomic coherence effects, such as near-resonant EIT [43–45,49], far-off resonant Raman process [46–48], and optical pumping [50–52]. Recent proposals for achieving optical nonreciprocity in atomic systems have also been explored based on atomic collision [53], atomic reservoir engineering [54], and four-wave mixing effect [55,56].

Compared with previous related studies, our work is motivated by two key aspects. First, our scheme enables independent manipulation of two counter-propagating probe pulses. The optical response of each probe pulse is independently controlled by its corresponding co-propagating control field, allowing flexible implementation of symmetric and asymmetric optical transport. Furthermore, when the forward and backward transparency windows are spectrally separated, the system exhibits frequency-tunable bidirectional nonreciprocity. Second, most previous studies have primarily focused on steady-state nonreciprocal responses and optimizing device performance, such as broad nonreciprocal bandwidths, high isolation ratios, and low insertion losses. In contrast, we investigate both the steady-state nonreciprocal spectra and the dynamical evolution of the two probe pulses, with particular emphasis on coherently controlled optical propagation, storage, and retrieval. To better reflect practical scenarios in optical communication and information processing, we consider Gaussian probe pulses rather than continuous-wave fields at a single frequency. Based on these considerations, we implement the scheme in a four-level tripod-type thermal atomic medium driven by two counter-propagating control fields. Probe pulses injected from opposite ends of the medium can undergo either symmetric or asymmetric propagation and storage, while

the transmission, group velocity, and storage of each pulse are determined mainly by the detuning and intensity of its co-propagating control field. Such independent asymmetric control is difficult to realize in a conventional reciprocal cold-atom medium without introducing additional nonreciprocal mechanisms. Our results provide a versatile platform for direction-dependent all-optical transport, storage, isolation, and routing of counter-propagating signals, and may be extended to multi-channel nonreciprocal photonic devices through the introduction of additional control fields.

2. Model and Equations

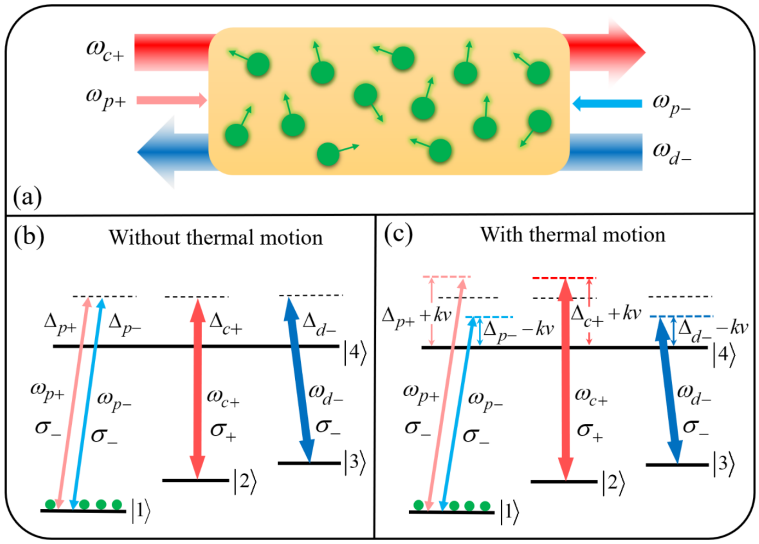


Fig. 1: (a) Diagram of a thermal ^{87}Rb atomic medium interacting with an FW coupling field ω_{c+} and a BW driving field ω_{d-}. A pair of counter-propagating probe pulses, ω_{p+} and ω_{p-}, are input from both ends of the medium, respectively. (b), (c) Simplified energy level diagrams of the tripod-type system without thermal motion (b) and with thermal motion (c). Level $|1\rangle$ corresponds to the Zeeman sublevels of the hyperfine state $\left|5S_{1/2}, F=1\right\rangle$; levels $|2\rangle$ and $|3\rangle$ correspond to the Zeeman sublevels of $\left|5S_{1/2}, F=2\right\rangle$; level $|4\rangle$ corresponds to the Zeeman sublevels of $\left|5P_{3/2}, F'=1\right\rangle$. σ_- and σ_+ represent the left and right circularly light polarizations, respectively.

Here, we consider a cloud of thermal ^{87}Rb atoms interacting with four laser fields to form an effective four-level tripod-type system, as shown in Fig. 1. The atomic cloud is modeled as a one-dimensional medium with length $L = 4.0$ mm and density $N = 4.0 \times 10^{12}$ cm^{-3}. Tripod-type atomic configurations have been widely investigated in previous theoretical and experimental studies [57–61]. The classical forward (FW) coupling field interacts with the transition $|2\rangle \leftrightarrow |4\rangle$ with the carrier frequency ω_{c+} and wave number k_{c+}, whereas the classical backward (BW) driving field couples the transition $|3\rangle \leftrightarrow |4\rangle$ with ω_{d-} and k_{d-}. The electric fields of two strong control fields can be expressed as:

$$\mathbf{E}_{\mathrm{c}+}(z,t) = \boldsymbol{\epsilon}_{\mathrm{c}+}\frac{E_{\mathrm{c}0}}{2}e^{-i\omega_{\mathrm{c}+}t+ik_{\mathrm{c}+}z},$$
$$\mathbf{E}_{\mathrm{d}-}(z,t) = \boldsymbol{\epsilon}_{\mathrm{d}-}\frac{E_{d0}}{2}e^{-i\omega_{\mathrm{d}-}t-ik_{\mathrm{d}-}z}. \tag{1}$$

The dipole-allowed transition $|1\rangle \leftrightarrow |4\rangle$ is probed, respectively, by the FW and BW classical weak probe fields

$$\mathbf{E}_{\mathrm{p}\pm}(z,t) = \boldsymbol{\epsilon}_{\mathrm{p}\pm}\frac{\widetilde{E}_{\mathrm{p}\pm}(z,t)}{2}e^{-i\omega_{\mathrm{p}\pm}t\pm ik_{\mathrm{p}\pm}z}. \tag{2}$$

The unit polarization vectors are given by $\boldsymbol{\epsilon}_{\mathrm{c}+,\mathrm{d}-,\mathrm{p}\pm}$. $\widetilde{E}_{\mathrm{p}\pm}(z,t)$ are the slowly varying classical electric-field envelopes of the probes.

The tripod-type atoms, on the other hand, are described by the matrix elements of collective atomic density operators

$$\sigma_{\alpha\beta}(z,t) \equiv \langle\alpha|\,\rho(z,t)\,|\beta\rangle\,, \qquad \{\alpha,\beta\} \in \{1,2,3,4\}. \tag{3}$$

In the interaction picture, the system evolution is governed by a set of reduced dynamic equations in the weak probe and adiabatic control limits:

$$\begin{aligned}
\dot{\sigma}_{21} &= -\gamma_{21}\sigma_{21} + i\Omega^{*}_{\mathrm{c}+}\sigma_{41}e^{i\Delta_{\mathrm{c}+}t-ik_{\mathrm{c}+}z},\\
\dot{\sigma}_{31} &= -\gamma_{31}\sigma_{31} + i\Omega^{*}_{\mathrm{d}-}\sigma_{41}e^{i\Delta_{\mathrm{d}-}t+ik_{\mathrm{d}-}z},\\
\dot{\sigma}_{41} &= -\gamma_{41}\sigma_{41} + i\Omega_{\mathrm{c}+}\sigma_{21}e^{-i\Delta_{\mathrm{c}+}t+ik_{\mathrm{c}+}z} + i\Omega_{\mathrm{d}-}\sigma_{31}e^{-i\Delta_{\mathrm{d}-}t-ik_{\mathrm{d}-}z}\\
&\quad + i\Omega_{\mathrm{p}+}e^{-i\Delta_{\mathrm{p}+}t+ik_{\mathrm{p}+}z} + i\Omega_{\mathrm{p}-}e^{-i\Delta_{\mathrm{p}-}t-ik_{\mathrm{p}-}z},
\end{aligned} \tag{4}$$

with $\gamma_{\alpha\beta}$ being the decay rate of atomic coherence on transition $|\alpha\rangle \leftrightarrow |\beta\rangle$ while $\Delta_{\mathrm{p}\pm}$, $\Delta_{\mathrm{c}+}$, and $\Delta_{\mathrm{d}-}$ being the probe, FW coupling, and BW driving frequency detunings from corresponding atomic transitions, respectively. Moreover, the half Rabi frequencies of the FW coupling, BW driving, and FW (BW) probe fields are $\Omega_{\mathrm{c}+} = E_{\mathrm{c}0}\boldsymbol{\epsilon}_{\mathrm{c}+}\cdot\mathbf{d}_{42}/(2\hbar)$, $\Omega_{\mathrm{d}-} = E_{\mathrm{d}0}\boldsymbol{\epsilon}_{\mathrm{d}-}\cdot\mathbf{d}_{43}/(2\hbar)$, and $\Omega_{\mathrm{p}\pm}(z,t) = \widetilde{E}_{\mathrm{p}\pm}(z,t)\boldsymbol{\epsilon}_{\mathrm{p}\pm}\cdot\mathbf{d}_{41}/(2\hbar)$, respectively, with $\mathrm{d}_{\alpha\beta}$ being the electric dipole matrix element for the transition $|\alpha\rangle \leftrightarrow |\beta\rangle$. For simplicity, the projected dipole matrix element $d_{\alpha\beta} = \boldsymbol{\epsilon}_i\cdot\mathbf{d}_{\alpha\beta}$ is used in the following derivations, where $\boldsymbol{\epsilon}_i$ is the polarization unit vector associated with the corresponding optical field interacting with the transition. The derivation from the semiclassical interaction Hamiltonian, including the weak-probe approximation, is given in Appendix A.

We should notice that when considering the atomic thermal motion, the FW and BW probe/control fields will be "seen" by atoms with different Doppler shifts, resulting in the need to alter the detunings of four laser fields ($\Delta_{\mathrm{p}+}$, $\Delta_{\mathrm{p}-}$, $\Delta_{\mathrm{c}+}$, $\Delta_{\mathrm{d}-}$) to ($\Delta_{\mathrm{p}+}+k_{\mathrm{p}+}v$, $\Delta_{\mathrm{p}-}-k_{\mathrm{p}-}v$, $\Delta_{\mathrm{c}+}+k_{\mathrm{c}+}v$, $\Delta_{\mathrm{d}-}-k_{\mathrm{d}-}v$). To simplify the situation, we use the assumption of $k_{\mathrm{p}+}\approx k_{\mathrm{p}-}\approx k_{\mathrm{c}+}\approx k_{\mathrm{d}-}=k$, which is reasonable since the wave vector mismatch in our system is minimal and the frequency differences among the four lasers

can be canceled by slightly misaligning the beams in the z-direction. Hence, we can rewrite Eq. (4) as

$$\begin{aligned}
\dot{\sigma}_{21} =& -\gamma_{21}\sigma_{21} + i\Omega_{\mathrm{c}+}^{*}\sigma_{41}e^{i(\Delta_{\mathrm{c}+}+kv)t-ikz},\\
\dot{\sigma}_{31} =& -\gamma_{31}\sigma_{31} + i\Omega_{\mathrm{d}-}^{*}\sigma_{41}e^{i(\Delta_{\mathrm{d}-}-kv)t+ikz},\\
\dot{\sigma}_{41} =& -\gamma_{41}\sigma_{41} + i\Omega_{\mathrm{c}+}\sigma_{21}e^{-i(\Delta_{\mathrm{c}+}+kv)t+ikz} + i\Omega_{\mathrm{d}-}\sigma_{31}e^{-i(\Delta_{\mathrm{d}-}-kv)t-ikz}\\
&+ i\Omega_{\mathrm{p}+}e^{-i(\Delta_{\mathrm{p}+}+kv)t+ikz} + i\Omega_{\mathrm{p}-}e^{-i(\Delta_{\mathrm{p}-}-kv)t-ikz}.
\end{aligned} \tag{5}$$

To eliminate the oscillation terms in Eq. (5), we further use a spatial Fourier expansion [62] and write the atomic coherences as

$$\begin{aligned}
\sigma_{21} =& \widetilde{\sigma}_{21}^{(0)}e^{-i(\Delta_{\mathrm{p}+}-\Delta_{\mathrm{c}+})t} + \widetilde{\sigma}_{21}^{(-2)}e^{-i(\Delta_{\mathrm{p}-}-\Delta_{\mathrm{c}+}-2kv)t-i2kz},\\
\sigma_{31} =& \widetilde{\sigma}_{31}^{(0)}e^{-i(\Delta_{\mathrm{p}-}-\Delta_{\mathrm{d}-})t} + \widetilde{\sigma}_{31}^{(+2)}e^{-i(\Delta_{\mathrm{p}+}-\Delta_{\mathrm{d}-}+2kv)t+i2kz},\\
\sigma_{41} =& \widetilde{\sigma}_{41}^{(+1)}e^{-i(\Delta_{\mathrm{p}+}+kv)t+ikz} + \widetilde{\sigma}_{41}^{(-1)}e^{-i(\Delta_{\mathrm{p}-}-kv)t-ikz}.
\end{aligned} \tag{6}$$

The superscripts (n) label spatial harmonics with wave vectors nk. All six amplitudes are first order in the probe fields. Since the two control fields couple different lower states to the excited state, these components form a closed set, as shown in Appendix A. Substituting Eq. (6) into Eq. (5), we can obtain a more concise Bloch equation for the atomic coherences:

$$\begin{aligned}
\dot{\widetilde{\sigma}}_{21}^{(0)} &= -G_{21}^{(0)}\widetilde{\sigma}_{21}^{(0)} + i\Omega_{\mathrm{c}+}^{*}\widetilde{\sigma}_{41}^{(+1)},\\
\dot{\widetilde{\sigma}}_{21}^{(-2)} &= -G_{21}^{(-2)}\widetilde{\sigma}_{21}^{(-2)} + i\Omega_{\mathrm{c}+}^{*}\widetilde{\sigma}_{41}^{(-1)},\\
\dot{\widetilde{\sigma}}_{31}^{(0)} &= -G_{31}^{(0)}\widetilde{\sigma}_{31}^{(0)} + i\Omega_{\mathrm{d}-}^{*}\widetilde{\sigma}_{41}^{(-1)},\\
\dot{\widetilde{\sigma}}_{31}^{(+2)} &= -G_{31}^{(+2)}\widetilde{\sigma}_{31}^{(+2)} + i\Omega_{\mathrm{d}-}^{*}\widetilde{\sigma}_{41}^{(+1)},\\
\dot{\widetilde{\sigma}}_{41}^{(+1)} &= -G_{41}^{(+1)}\widetilde{\sigma}_{41}^{(+1)} + i\Omega_{c+}\widetilde{\sigma}_{21}^{(0)} + i\Omega_{\mathrm{d}-}\widetilde{\sigma}_{31}^{(+2)} + i\Omega_{\mathrm{p}+},\\
\dot{\widetilde{\sigma}}_{41}^{(-1)} &= -G_{41}^{(-1)}\widetilde{\sigma}_{41}^{(-1)} + i\Omega_{\mathrm{c}+}\widetilde{\sigma}_{21}^{(-2)} + i\Omega_{\mathrm{d}-}\widetilde{\sigma}_{31}^{(0)} + i\Omega_{\mathrm{p}-},
\end{aligned} \tag{7}$$

where the complex dephasing rates are defined as follows: $G_{21}^{(0)} = \gamma_{21} - i\left(\Delta_{\mathrm{p}+} - \Delta_{\mathrm{c}+}\right)$, $G_{21}^{(-2)} = \gamma_{21} - i\left(\Delta_{p-} - \Delta_{c+} - 2kv\right)$, $G_{31}^{(0)} = \gamma_{31} - i\left(\Delta_{\mathrm{p}-} - \Delta_{\mathrm{d}-}\right)$, $G_{31}^{(+2)} = \gamma_{31} - i\left(\Delta_{\mathrm{p}+} - \Delta_{\mathrm{d}-} + 2kv\right)$, and $G_{41}^{(\pm 1)} = \gamma_{41} - i(\Delta_{\mathrm{p}\pm} \pm kv)$. From Eq. (7), we find that the system evolution is determined by the first-order components of collective atomic photonic coherences $[\widetilde{\sigma}_{41}^{(+1)}, \widetilde{\sigma}_{41}^{(-1)}]$, and together the zero- and second-order atomic spin coherences $[\widetilde{\sigma}_{21}^{(0)}, \widetilde{\sigma}_{31}^{(0)}]$ and $[\widetilde{\sigma}_{21}^{(-2)}, \widetilde{\sigma}_{31}^{(+2)}]$. The zero-order spin coherences arise from the two-photon resonance between the probe and control fields in the same direction, resulting in transparency. The second-order coherences arise from counter-propagating probe–control pairs and have a two-photon Doppler mismatch of order $2kv$. Their contribution is strongly suppressed by velocity averaging but is retained in the complete calculation.

When the contributions from atoms moving at various velocities are taken into account, the total linear susceptibility average over the velocity distribution for the FW probe can be written as

$$\chi_F = \frac{|d_{41}|^2}{\varepsilon_0\hbar}\int_{-\infty}^{+\infty}\frac{N(v)\widetilde{\sigma}_{41}^{(+1)}(v)}{\Omega_{\mathrm{p}+}}dv. \tag{8}$$

Here the thermal atoms satisfy Maxwell-Boltzmann velocity distribution $N(v) = Ne^{-v^2/v_p^2}/(v_p\sqrt{\pi})$, where $v_p = \sqrt{2k_{\rm B}T/m}$ is the most probable velocity with $k_{\rm B}$ being the Boltzmann constant, T the temperature of the atomic gas, and m the atomic mass. Similar to this, the BW linear susceptibility becomes

$$\chi_B = \frac{|d_{41}|^2}{\varepsilon_0\hbar}\int_{-\infty}^{+\infty}\frac{N(v)\widetilde{\sigma}_{41}^{(-1)}(v)}{\Omega_{\rm p-}}dv. \tag{9}$$

To precisely elucidate how the optical nonreciprocity performs, we quantitatively define some transmission parameters of the probe fields as the FW/BW transmission $T_{\rm F,B} = \exp[-{\rm Im}(\chi_{F,B})kL]$, the transmission contrast $C_{\rm FB} = (T_{\rm F} - T_{\rm B})/(T_{\rm F} + T_{\rm B})$, the isolation ratio $I_{\rm FB} = 10\log_{10}(T_{\rm F}/T_{\rm B})$, and the insertion loss of an allowed channel ${\rm IL}_{\rm F,B} = -10\log_{10}T_{\rm F,B}$. Furthermore, to study the propagation dynamics of the probe envelopes, we also need the following Maxwell equation:

$$\begin{aligned}\left(\frac{\partial}{\partial t} + c\frac{\partial}{\partial z}\right)\Omega_{\rm p+}(z,t) &= i\eta_{\rm p+}\int_{-\infty}^{+\infty}N(v)\widetilde{\sigma}_{41}^{(+1)}(v)dv,\\ \left(\frac{\partial}{\partial t} - c\frac{\partial}{\partial z}\right)\Omega_{\rm p-}(z,t) &= i\eta_{\rm p-}\int_{-\infty}^{+\infty}N(v)\widetilde{\sigma}_{41}^{(-1)}(v)dv,\end{aligned} \tag{10}$$

Here $\eta_{\rm p\pm} = \omega_{\rm p\pm}|d_{41}|^2/(2\varepsilon_0\hbar)$, and Eq. (10) follows from the slowly varying envelope approximation. We calculate the transmission spectra based on the steady-state FW and BW linear susceptibilities of Eqs. (8) and (9) and investigate the dynamic evolution of two probe pulses based on the coupled Maxwell-Bloch approach of Eqs. (7) and (10). The probe intensities are normalized to the corresponding peak incident probe intensities. For either directional component, the normalized probe intensity is defined as $|\Omega_{\rm p\pm}(z,t)/\Omega_{\rm p\pm}^0|^2 = |\widetilde{E}_{\rm p\pm}(z,t)/\widetilde{E}_{\rm p\pm}^0|^2$. Here $\Omega_{\rm p\pm}^0$ and $\widetilde{E}_{\rm p\pm}^0$ denote the peak half Rabi frequency and peak electric-field envelope of the corresponding incident probe pulse, respectively. It is worth mentioning that the probe transmission can be analyzed using the dynamic method by calculating the ratio of output pulse energy to the input one. Here we choose the steady-state method because the dynamic method is much more time-consuming due to the Doppler integral when we consider an average over all the atoms in the velocity distribution. For a long probe pulse, the dynamic transmission is almost consistent with the steady-state transmission of a continuous light whose frequency is equal to the central frequency of the probe pulse. Therefore, we choose to first examine the steady-state transmission spectra to facilitate the subsequent exploration of the dynamic evolution of the probe pulses, i.e., we can refer to the steady-state spectra to achieve various dynamic propagation and storage schemes by selecting specific parameters for the four light fields.

3. Results and Discussions

Based on the theoretical analysis, we demonstrate various control schemes for a pair of counter-propagating probe pulses by modulating the two counter-propagating control fields in a thermal atomic medium. Here, we use thermal atoms at $T = 1.0$ K as a representative operating condition for the propagation and storage examples below. Although the DE at $T = 1.0$ K is less significant than that at room temperature, the Doppler broadening obtained here is sufficient to generate optical nonreciprocity for implementing our schemes.

Initially, we consider the case where we turn off the BW driving (FW coupling) field and keep the FW coupling (BW driving) field active. The four-level response can then be approximated by a three-level Λ channel, denoted as FW-Λ (BW-Λ), which permits transmission of the FW (BW) probe field along the $+z$ ($-z$) direction. This behavior arises from the DE-free two-photon resonance for the FW (BW) probe pulse and the DE-enhanced two-photon non-resonance for the opposite pulse [9]. Consequently, the FW-allowed isolator and BW-allowed isolator can be easily toggled by simply turning off one of the two control fields. Alternatively, when we turn on two control fields with equal detunings and Rabi frequencies, the FW and BW transmission windows are identical, which allows the bidirectional propagation of a probe pulse with the center frequency inside this window. The four-level system can no longer function as an optical isolator due to the loss of nonreciprocity. In this configuration, if we input a pair of probe pulses from two opposite ends of the medium respectively, they will travel through the medium in the same way except in opposite directions.

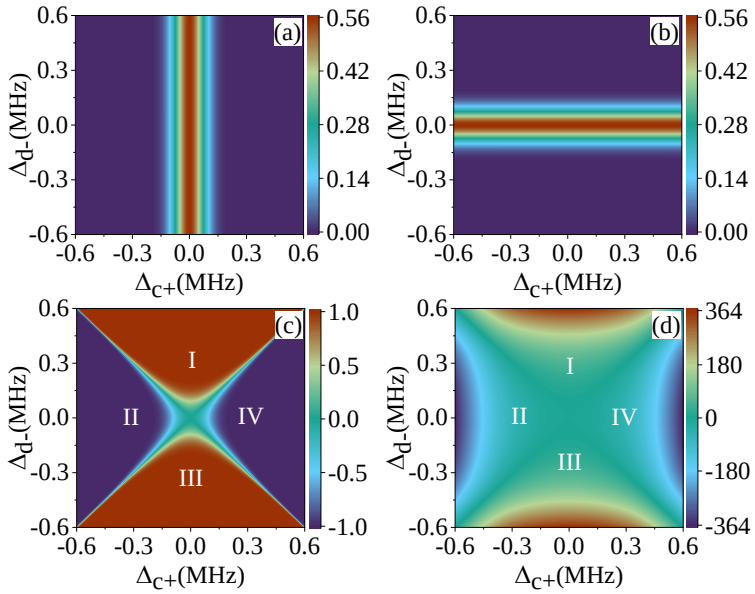


Fig. 2: (a) The FW transmission $T_{\rm F}$, (b) the BW transmission $T_{\rm B}$, (c) the transmission contrast $C_{\rm FB}$, and (d) the isolation ratio $I_{\rm FB}$ versus $\Delta_{\rm c+}$ and $\Delta_{\rm d-}$ for two on-resonance probe fields with $\Delta_{\rm p+} = \Delta_{\rm p-} = 0$ MHz. Other relevant parameters are $L = 4.0$ mm, $N = 4.0 \times 10^{12}$ cm^{-3}, $T = 1.0$ K, $\gamma_{41} = 6.0$ MHz, $\gamma_{21} = \gamma_{31} = 2.0$ kHz, and $\Omega_{\rm c+} = \Omega_{\rm d-} = 4.0$ MHz.

To investigate the influence of the control field detunings $\Delta_{\rm c+,d-}$ on the transmission spectra $T_{\rm F}$ and $T_{\rm B}$, we assume that the center frequencies of the FW and BW probe fields are both resonant with the atomic transition $|1\rangle \leftrightarrow |4\rangle$, i.e., $\Delta_{\rm p+} = \Delta_{\rm p-} = 0$ MHz. Figures 2(a) and 2(b) show respectively $T_{\rm F}$ and $T_{\rm B}$ as a function of $\Delta_{\rm c+}$ and $\Delta_{\rm d-}$. In Fig. 2(a), a narrow transmission window of $T_{\rm F}$ is located around $\Delta_{\rm c+} = 0$, corresponding to the two-photon resonance position $\Delta_{\rm p+} - \Delta_{\rm c+} = 0$, regardless of Δ_{d-}. Similarly, in Fig. 2(b), the $T_{\rm B}$ transmission window appears near the BW two-photon resonance position $\Delta_{\rm p-} - \Delta_{\rm d-} = 0$ and remains unaffected by $\Delta_{\rm c+}$. These findings provide clear evidence for the independence of FW (BW) probe transmission from the BW driving field $\Omega_{\rm d-}$ (the FW coupling field $\Omega_{\rm c+}$).

This conclusion can be directly inferred from Eq. (7). The FW transmission $T_{\rm F}$, mediated by the photonic coherence $\widetilde{\sigma}_{41}^{(+1)}$, is primarily related to the spin coherence $\widetilde{\sigma}_{21}^{(0)}$ induced by $\widetilde{E}_{\rm p+}(z,t)$ and $\Omega_{\rm c+}$, as well as $\widetilde{\sigma}_{31}^{(+2)}$ induced by $\widetilde{E}_{\rm p+}(z,t)$ and $\Omega_{\rm d-}$. However, the two-photon resonance condition between $\widetilde{E}_{\rm p+}(z,t)$ with $(\Delta_{\rm p+}+kv)$ and $\Omega_{\rm d-}$ with $(\Delta_{\rm d-}-kv)$ is broken due to the opposite Doppler shifts. Hence, after Doppler averaging, the influence of $\widetilde{\sigma}_{31}^{(+2)}$ on $T_{\rm F}$ is much weaker than that of $\widetilde{\sigma}_{21}^{(0)}$. Similarly, $\widetilde{\sigma}_{21}^{(-2)}$ induced by $\widetilde{E}_{\rm p-}(z,t)$ and $\Omega_{\rm c+}$ produces a negligible impact on $T_{\rm B}$ compared to $\widetilde{\sigma}_{31}^{(0)}$ induced by $\widetilde{E}_{\rm p-}(z,t)$ and $\Omega_{\rm d-}$. This is due to the opposite Doppler shifts between $\widetilde{E}_{\rm p-}(z,t)$ with $(\Delta_{\rm p-}-kv)$ and $\Omega_{\rm c+}$ with $(\Delta_{\rm c+}+kv)$. Combining Eqs. (7) and (10), we can conclude that the dynamic evolution of $\widetilde{E}_{\rm p+}(z,t)$ $[\widetilde{E}_{\rm p-}(z,t)]$ across the medium, mediated by $\widetilde{\sigma}_{41}^{(+1)}$ $[\widetilde{\sigma}_{41}^{(-1)}]$, is mainly determined by $\widetilde{\sigma}_{21}^{(0)}$ $[\widetilde{\sigma}_{31}^{(0)}]$, because $\widetilde{\sigma}_{31}^{(+2)}$ $[\widetilde{\sigma}_{21}^{(-2)}]$ is small enough to be safely ignored. Therefore, this tripod system can be viewed as a simple three-level FW-Λ EIT system for the FW probe and a BW-Λ system for the BW probe. A useful weak-mixing condition is that the characteristic counter-propagating two-photon Doppler scale $\delta_{\rm 2D}=2kv_p$ exceed the power-broadened Raman linewidth $\Gamma_{\rm EIT}\simeq\gamma_g+|\Omega|^2/\gamma_{41}$, where $\gamma_g=\gamma_{21}=\gamma_{31}$ is the ground-state coherence dephasing rate for the present parameters. For the present parameters, $\delta_{\rm 2D}=35.47$ MHz, whereas $\Gamma_{\rm EIT}\simeq 2.67$ MHz and $|\Omega_{\rm c+}|=|\Omega_{\rm d-}|=4.0$ MHz. Thus, the two channels are effectively separated within the near-resonant bandwidth.

The transmission contrast $C_{\rm FB}$ and isolation ratio $I_{\rm FB}$ are displayed in Figs. 2(c) and 2(d), respectively, where the positive values represent the cases of $T_{\rm F}>T_{\rm B}$, and the negative values indicate $T_{\rm F}<T_{\rm B}$. We can divide Fig. 2(c) [Fig. 2(d)] into four regions with two diagonal lines. In regions I and III, $T_{\rm F}>T_{\rm B}$, while in regions II and IV, $T_{\rm F}<T_{\rm B}$. Along the two diagonal lines of Fig. 2(c) [Fig. 2(d)], all the transmission contrasts and isolation ratios are equal to zero, because two control fields have equal detuning magnitudes there, i.e., $|\Delta_{\rm c+}|=|\Delta_{\rm d-}|$ satisfy $\Delta_{\rm c+}=\pm\Delta_{\rm d-}$, leading to the total overlap or symmetric distribution of $T_{\rm F}$ and $T_{\rm B}$ windows. Particularly, the intersection point of the two diagonal lines, i.e., $\Delta_{\rm c+}=\Delta_{\rm d-}=0$ MHz, represents the symmetric case with the maximal FW and BW transmissions (55.7%) for the two on-resonant probes. In the middle green region surrounding the central position in Fig. 2(c) [Fig. 2(d)], both the FW and BW probes can propagate through the medium.

According to Fig. 2, we can realize various propagation scenarios for two counter-propagating probe pulses by modulating $\Delta_{\rm c+}$ and $\Delta_{\rm d-}$. Here, we input two Gaussian probe pulses with envelopes $\widetilde{E}_{\rm p\pm}^{\rm in}(t)=\widetilde{E}_{\rm p\pm}^{0}e^{-(t-t_0)^2/(2\tau^2)}$, where $t_0=16.0$ μs and $\tau=6.0$ μs. The relatively long probe pulses ensure that the dependence of the dynamic pulse transmission on $\Delta_{\rm c+}$ and $\Delta_{\rm d-}$ is almost consistent with the steady-state transmission spectra in Fig. 2. In Fig. 3(a), when $\Omega_{\rm c+}=\Omega_{\rm d-}=4.0$ MHz and $\Delta_{\rm c+}=\Delta_{\rm d-}=0$ MHz, both the FW and BW probes, satisfying their respective two-photon resonance conditions, can pass through the sample with the same velocity and transmission but in opposite directions. The peak intensity of the FW (BW) output pulse is 52.6% relative to the input pulse, which is slightly smaller than the maximal FW (BW) transmission value of 55.7% as shown in Fig. 2. This is because the frequency bandwidth of the FW (BW) probe pulse is marginally wider than that of the FW (BW) transmission window. When propagating through the medium, the probe pulses are partially absorbed. This discrepancy can

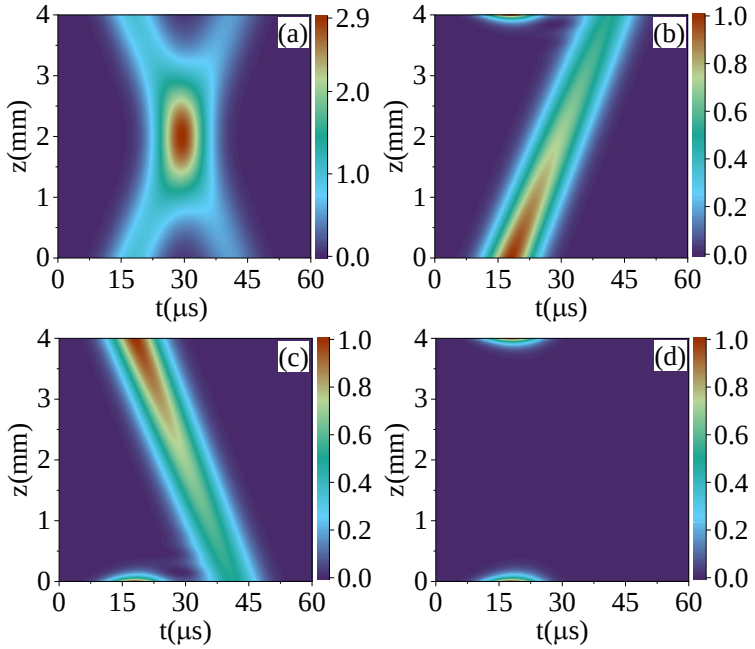


Fig. 3: Dynamic evolution of the FW and BW probe pulses incident from $z = 0$ and $z = L$ of the medium when we set different detunings for two control fields. (a) $\Delta_{c+} = \Delta_{d-} = 0$ MHz; (b) $\Delta_{c+} = 0$ MHz, $\Delta_{d-} = 0.5$ MHz; (c) $\Delta_{c+} = 0.5$ MHz, $\Delta_{d-} = 0$ MHz; (d) $\Delta_{c+} = \Delta_{d-} = 0.5$ MHz. Other parameters are the same as in Fig. 2.

be eliminated by adopting probe pulses with longer temporal durations so that all the probe frequency components are distributed around the transmission peaks. In the unidirectional traveling case shown in Fig. 3(b) [Fig. 3(c)], we set $\Delta_{c+} = 0$ MHz and $\Delta_{d-} = 0.5$ MHz ($\Delta_{c+} = 0.5$ MHz and $\Delta_{d-} = 0$ MHz) to fulfill the requirement of high transmission, i.e., 52.6% at the peak location, for the FW (BW) probe and zero transmission for the BW (FW) probe. In the case of bidirectional blockade, as shown in Fig. 3(d), we simultaneously tune Δ_{c+} and Δ_{d-} to 0.5 MHz. Both probes are prohibited from traveling through the medium since they fall outside their transmission windows.

It is worth noting that, as shown in Figs. 3(b) and 3(c), our system enables the realization of a frequency-tunable bidirectional optical isolator by appropriately selecting the control-field parameters. To further elucidate this bidirectional nonreciprocity, we can adopt the parameters of Fig. 3(b) [Fig. 3(c)] in Figs. 4(a-c) [Figs. 4(d-f)]. For simplicity, hereafter when assuming $\Delta_{p+} = \Delta_{p-}$, we use $\Delta_{p\pm} = \Delta_p$. As observed in Fig. 4(a) [Fig. 4(d)], there is no frequency overlap between the T_F and T_B windows. A probe pulse can propagate forward/backward along the medium within the T_F/T_B transmission window. By appropriately tuning the detunings of the two control fields, the FW-allowed and BW-allowed isolation bands can be shifted independently. This feature enables our system to operate as a frequency-tunable bidirectional optical isolator. The corresponding transmission contrast and isolation ratio are further illustrated in Figs. 4(b) and 4(c) [Figs. 4(e) and 4(f)]. As illustrated in Figs. 4(b) and 4(e), the FW-allowed (BW-allowed) isolation band corresponds to $C_{FB} = 1.0$ ($C_{FB} = -1.0$). Furthermore, Figs. 4(c) and 4(f) identify the frequency regions with large isolation ratios, providing the optimal operating bands for

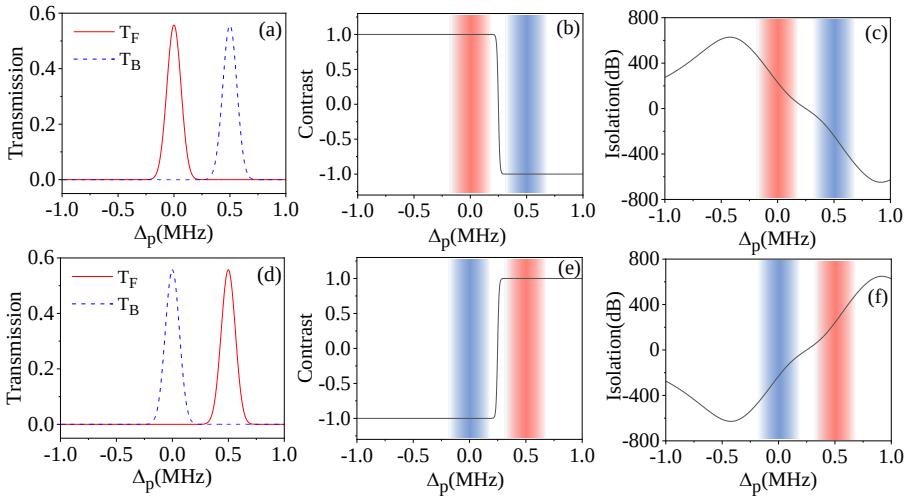


Fig. 4: The steady-state transmission spectra of bidirectional nonreciprocity. (a), (d) The FW and BW transmissions, (b), (e) the contrast, and (c), (f) the isolation ratio. In (a-c), $\Delta_{c+} = 0$ MHz and $\Delta_{d-} = 0.5$ MHz, i.e., the same case as shown in Fig. 3(b); in (d-f), $\Delta_{c+} = 0.5$ MHz and $\Delta_{d-} = 0$ MHz, i.e., the same case as shown in Fig. 3(c). The ranges of the FW and BW transmission windows are respectively marked with red and blue shades in (b), (c), (e), and (f) for comparison. Other parameters are the same as in Fig. 2.

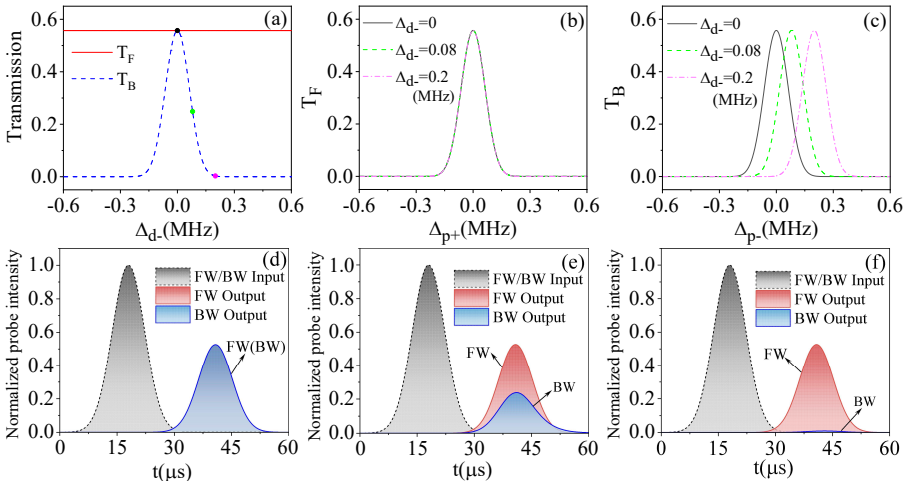


Fig. 5: (a) The FW and BW transmissions versus Δ_{d-} when $\Delta_{c+} = \Delta_{p+} = \Delta_{p-} = 0$ MHz. (b) The FW transmission versus Δ_{p+} and (c) the BW transmission versus Δ_{p-} with $\Delta_{d-} = 0$ MHz (black solid curve), $\Delta_{d-} = 0.08$ MHz (green dashed curve), and $\Delta_{d-} = 0.2$ MHz (magenta dash-dotted curve), respectively. (d),(e),(f) The input and output probe pulses under the three cases with $\Delta_{d-} = 0$ MHz in (d), 0.08 MHz in (e), and 0.2 MHz in (f). The red and blue solid curves represent the output FW and BW probes at the $z = L$ and $z = 0$ of the medium, respectively. The black dotted curve represents both the incident FW and BW probe pulses for reference. Other relevant parameters are the same as in Fig. 2.

efficient bidirectional optical isolation. The usable isolation band is defined as the continuous frequency interval around the allowed-channel resonance for which the directional isolation is at least 20 dB (a power ratio of 100) and the allowed-channel insertion loss does not exceed 3 dB ($T_{\mathrm{allowed}} \gtrsim 0.50$). Both the FW-allowed configuration in Figs. 4(a–c) and the BW-allowed configuration in Figs. 4(d–f) have a usable bandwidth of 0.0582 MHz, extending from −0.0291 to 0.0291 MHz relative to the allowed-channel resonance. At the band center, $T_{\mathrm{allowed}} = 0.557$, corresponding to an insertion loss of 2.54 dB. The blocked channel remains strongly suppressed over a broader frequency range, while the usable bandwidth is mainly limited by the EIT transmission window of the allowed channel. It is worth emphasizing that the successful implementation of this bidirectional optical isolator requires the complete separation of the T_{F} and T_{B} windows. Otherwise, the system would permit bidirectional propagation of a probe pulse within the overlapped FW and BW transmission range, thereby destroying the nonreciprocity.

To illustrate the transition from bidirectional to unidirectional propagation, we further investigate the case with $\Delta_{\mathrm{c}+} = 0$ MHz and $\Delta_{\mathrm{d}-}$ gradually varied. We plot the FW and BW transmissions versus $\Delta_{\mathrm{d}-}$ in Fig. 5(a), where T_{F} (red solid line) maintains the maximal value of 55.7%, while T_{B} (blue dashed curve) decreases rapidly with the increase of $|\Delta_{\mathrm{d}-}|$. We consider three specific cases with $\Delta_{\mathrm{d}-} = 0$ MHz (black dot), 0.08 MHz (green dot), and 0.2 MHz (magenta dot), as examples for further analysis. T_{B} is reduced from 55.7% to 24.9% and 0.2% at the position $\Delta_{\mathrm{p}-} = 0$ MHz. In the full tripod model, sweeping the cross-control Rabi frequency $|\Omega_{\mathrm{d}-}|$ from 0 to 8.0 MHz changes the resonant T_{F} by only 0.023%. For the $\tau = 6.0$ μs Gaussian probe used below, the pulse-spectrum-weighted FW transmission differs by 0.46% between the full tripod response and the effective FW-Λ response. The mirror BW configuration gives the same result. These results support the effective channel decomposition near resonance. We retain the complete Eq. (7) because the approximation becomes less accurate in the spectral wings. The corresponding T_{F} and T_{B} windows under these three conditions are illustrated in Figs. 5(b) and 5(c), respectively. By slightly adjusting $\Delta_{\mathrm{d}-}$ to deviate from the resonant position, the T_{F} window is unchanged [see Fig. 5(b)], but the T_{B} window moves to the right side, i.e., the two-photon resonant position $\Delta_{\mathrm{p}-} = \Delta_{\mathrm{d}-}$ [see Fig. 5(c)]. The temporal evolution processes of the two probes under these three conditions are shown in Figs. 5(d-f), respectively. It can be clearly observed that the normalized output intensity of the FW probe remains the same, whereas the normalized output intensity of the BW probe decreases with the increase of $|\Delta_{\mathrm{d}-}|$. The identical and different output intensities for forward and backward propagation shown in Figs. 5(d-f) verify again that our system can be used to realize optical transport devices with symmetric and asymmetric propagation characteristics.

Having demonstrated the tunable nonreciprocal propagation by adjusting the control field detunings, we further examine the temperature dependence of the nonreciprocal response at the representative FW-allowed operating point $\Delta_{c+} = 0$ MHz and $\Delta_{d-} = 0.5$ MHz in Fig. 6. The two probes remain on resonance, $\Delta_{\mathrm{p}+} = \Delta_{\mathrm{p}-} = 0$ MHz. In this temperature-dependent calculation, T enters only through the normalized Maxwell–Boltzmann velocity distribution. We keep the atomic density N and the dephasing rates γ_{41}, γ_{21}, and γ_{31} fixed to isolate thermal Doppler broadening. As shown in Fig. 6, in the absence of thermal

motion ($T = 0$), the two directions are reciprocal, with $T_{\mathrm{F}} = T_{\mathrm{B}} = 0.557$ and $C_{\mathrm{FB}} = 0$. Increasing T suppresses the BW transmission, and C_{FB} rapidly approaches unity on the sub-mK temperature scale and remains nearly saturated at higher temperatures. Over the range from 1 K to 300 K, the FW transmission remains approximately 0.557, whereas the BW transmission is negligible. Exchanging $\Delta_{\mathrm{c}+}$ and $\Delta_{\mathrm{d}-}$ gives the corresponding BW-allowed response by directional symmetry. This result shows that the steady-state Doppler-induced nonreciprocity persists up to room temperature within the fixed-density model. A complete equilibrium-vapor-cell model would also require temperature-dependent density and dephasing.

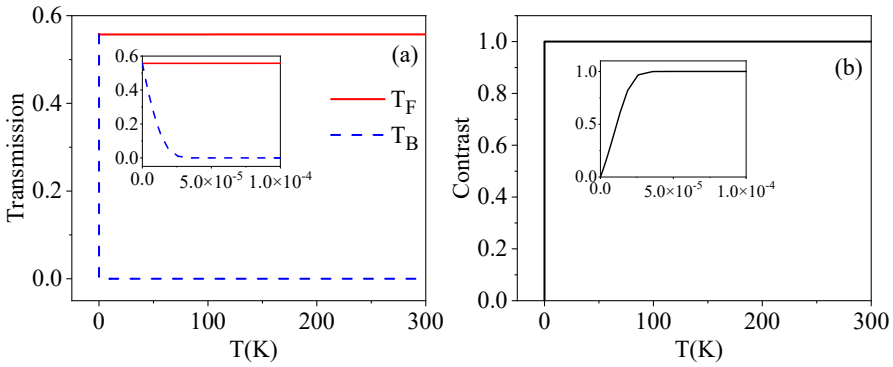


Fig. 6: Temperature dependence of (a) the FW and BW transmissions T_{F} and T_{B} and (b) the transmission contrast C_{FB} at the representative FW-allowed operating point $\Delta_{\mathrm{p}+} = \Delta_{\mathrm{p}-} = \Delta_{\mathrm{c}+} = 0$ MHz and $\Delta_{\mathrm{d}-} = 0.5$ MHz. The insets enlarge the low-temperature interval $0 \leq T \leq 1.0 \times 10^{-4}$ K. The atomic density is fixed at $N = 4.0 \times 10^{12}$ cm^{-3}, and all the other parameters are the same as in Fig. 2.

Next, we will investigate how symmetric and asymmetric light propagation and storage schemes can be realized by varying two control field intensities. In this system, the FW and BW probes can be transmitted and stored approximately independently as long as they satisfy the FW and BW two-photon resonance conditions. It is easy to find that the symmetric light propagation occurs when $\Omega_{\mathrm{c}+} = \Omega_{\mathrm{d}-}$ and $\Delta_{\mathrm{p}+} - \Delta_{\mathrm{c}+} = \Delta_{\mathrm{p}-} - \Delta_{\mathrm{d}-} = 0$. Otherwise, asymmetric propagation occurs. Figure 7(a) depicts the dynamic evolution of two counter-propagating probes traveling with different velocities and transmissions when we set unequal time-invariant Rabi frequencies: $\Omega_{\mathrm{c}+} = 4.0$ MHz and $\Omega_{\mathrm{d}-} = 5.0$ MHz. In Fig. 7(b), displaying the FW and BW output probes, the group velocity and the transmitted intensity of the BW probe are both larger than those of the FW probe. To gain a clear understanding of the mechanism, we present the corresponding FW and BW transmissions in Fig. 7(c), where the T_{B} window exhibits a larger amplitude and a broader width than the T_{F}. In the EIT regime, a higher transmission is always accompanied by a weaker slow-light effect. So it is necessary to strike a balance between these two competing requirements, slow velocity and high transmission, by appropriately selecting $\Omega_{\mathrm{c}+}$ and $\Omega_{\mathrm{d}-}$.

Finally, we demonstrate two-channel approximately independent storage and retrieval of the FW and BW probe pulses by temporally controlling their corresponding co-propagating control fields. In Fig. 8, we show the asymmetric storage processes using two different time modulations for the two control fields. In Figs. 8(a) and 8(b), we initially turn on $\Omega_{\mathrm{c}+} = \Omega_{\mathrm{d}-} = 4.0$ MHz to offer the EIT-based slow-light

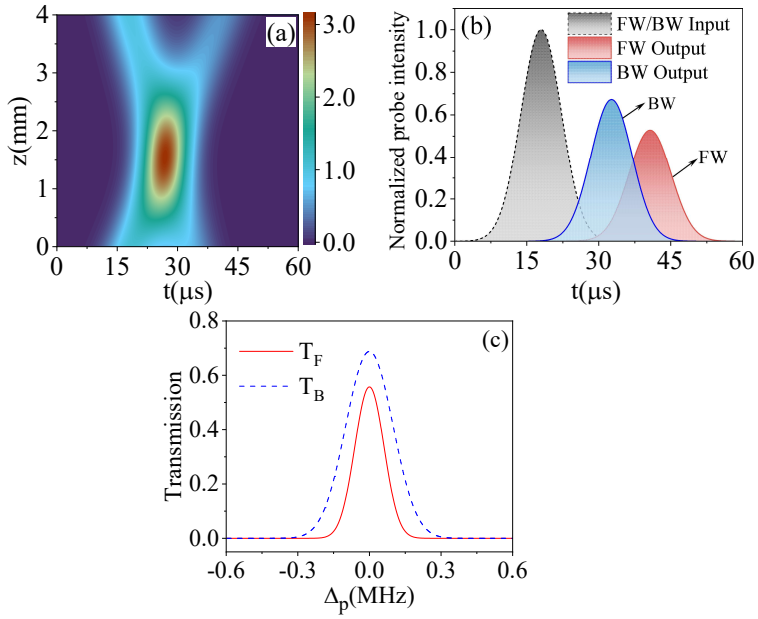


Fig. 7: (a) Asymmetric dynamic propagation of the FW and BW on-resonance probe pulses. (b) The input and output probes pulses corresponding to (a). (c) The FW (red solid curve) and BW (blue dashed curve) transmissions versus $\Delta_{\rm p}$. Here $\Delta_{\rm c+}=\Delta_{\rm d-}=0$ MHz, $\Omega_{\rm c+}=4.0$ MHz, $\Omega_{\rm d-}=5.0$ MHz, and other parameters are the same as in Fig. 2.

propagation scenarios for the two probe pulses. By adiabatically switching off $\Omega_{\rm c+}$ at 30.0 μs, the FW pulse disappears [see Fig. 8(a)], which means it is successfully stored into the atomic medium as the collective atomic spin coherence $\widetilde{\sigma}_{21}^{(0)}$. After a storage duration of 6.0 μs, we can retrieve the FW probe on demand by turning on $\Omega_{\rm c+}$. During the whole procedure, the BW probe continues traveling along the medium since $\Omega_{\rm d-}=4.0$ MHz is maintained. The delay time between the FW and BW output pulses, as depicted in Fig. 8(b), is due to the storage duration of the FW pulse. In Figs. 8(c) and 8(d), the second time modulation of control fields is implemented, where the FW probe is written into the atomic spin-wave $\widetilde{\sigma}_{21}^{(0)}$ during 30.0 μs $\rightarrow$ 36.0 μs, while the BW probe is trapped inside the medium as $\widetilde{\sigma}_{31}^{(0)}$ during 30.0 μs $\rightarrow$ 42.0 μs. Consequently, in Fig. 8(d), the BW output pulse is delayed compared to the FW output pulse due to a longer storage duration. We estimate the overall storage-and-retrieval energy efficiency as $\eta_{\rm SR}^{(\pm)}=\int_{t_{\rm r,\pm}}^{t_{\rm f}}|\widetilde{E}_{\rm p\pm}^{\rm out}(t)|^2dt/\int_0^{t_{\rm f}}|\widetilde{E}_{\rm p\pm}^{\rm in}(t)|^2dt$, where $t_{\rm r,\pm}$ is the time at which the corresponding control field is restored and $t_{\rm f}$ is the end time of the record. This definition gives the overall write–store–read efficiency by comparing the retrieved energy with the input energy, while excluding pre-storage leakage from the retrieved signal. The retrieved FW pulse in Figs. 8(a,b) has $\eta_{\rm SR}^{(+)}=45.89\%$. In Figs. 8(c,d), the FW and BW efficiencies are 45.13% and 39.08%, respectively. The lower BW value is consistent with its longer storage interval. These quantities characterize the storage and retrieval at the semiclassical mean-field level. The reversible transfer between the photonic component $\widetilde{E}_{\rm p+}(z,t)$ [$\widetilde{E}_{\rm p-}(z,t)$] and atomic spin coherence $\widetilde{\sigma}_{21}^{(0)}$ [$\widetilde{\sigma}_{31}^{(0)}$] can be precisely controlled by manipulating the switching sequence of $\Omega_{\rm c+}$ ($\Omega_{\rm d-}$). Throughout the storage and retrieval processes, the strong control fields are established before the

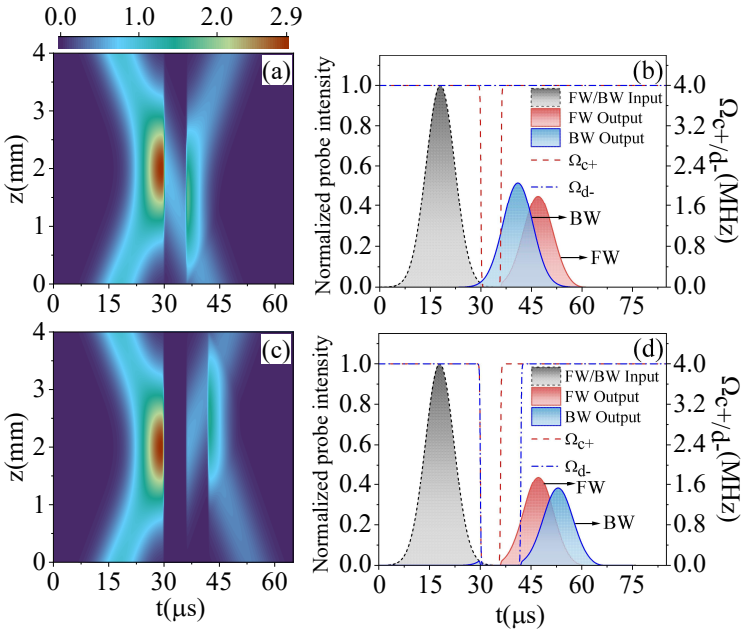


Fig. 8: Asymmetric light storage and retrieval of the FW and BW probe pulses. (a) The FW probe is stored at 30.0 μs and retrieved at 36.0 μs, while the BW probe propagates directly out of the medium. (c) The FW probe is stored at 30.0 μs and retrieved at 36.0 μs, while the BW probe is stored at 30.0 μs and retrieved at 42.0 μs. (b) and (d) The FW and BW input and output probes corresponding to (a) and (c), respectively. The red dashed and blue dash-dotted curves indicate the time-varying diagrams of the FW and BW control fields, respectively. Here $\Delta_{\mathrm{p}\pm} = \Delta_{\mathrm{c}+} = \Delta_{\mathrm{d}-} = 0$ MHz, and other parameters are the same as in Fig. 2.

arrival of the weak probe pulses and are switched on and off sufficiently slowly to satisfy the adiabatic EIT condition, ensuring that the probe spectra remain within the corresponding transparency windows [63,64]. Accordingly, we can flexibly store the two probes in a desired asymmetric way, such as at different moments, for different periods, or in different locations of the medium. However, the symmetric storage scheme requires identical intensities and time modulations for both control fields. It is worth pointing out that all the asymmetric control methods mentioned above cannot be accomplished in a regular cold tripod-type atomic system, where both probe pulses have the same transmissions and group velocities regardless of their propagation directions.

For an experimental implementation, the tripod manifold can be constructed from hyperfine–Zeeman sublevels of the ^{87}Rb D2 line near 780 nm. In this configuration, each probe field, together with its corresponding control field, defines an optical channel, and the two probe-control field pairs constitute the dual-channel configuration considered in this work. Related experiments in Rb have separately demonstrated tripod EIT and light storage, as well as thermal-motion-induced optical nonreciprocity [9,59,60], supporting the experimental feasibility of the main ingredients of our scheme. In practice, parameters such as the atomic density and dephasing rates may vary with temperature. Such temperature-dependent variations are not explicitly included in the present model and may affect the transmission and isolation contrast in an experimental implementation. Beyond the present dual-channel configuration, the scheme may, in principle, be extended to more channels by employing additional long-lived hyperfine–Zeeman states and optical coupling fields, although the achievable channel number is constrained by the available atomic level structure and selection rules.

4. Conclusion

We have presented an intriguing scheme for implementing symmetric and asymmetric manipulations for two counter-propagating probe pulses in a four-level tripod-type thermal atomic sample driven by two counter-propagating control fields. This scheme relies on dynamically controlled dual-channel optical nonreciprocity induced by atomic thermal motion. Due to the Doppler shifts, this tripod system can be treated as two approximately independent three-level Λ-type systems. The FW-Λ (BW-Λ) system provides the EIT scenario and is mainly responsible for the propagation and storage of the FW (BW) probe. The symmetric modulation requires equal control-field intensities and two-photon resonance in both FW-Λ and BW-Λ systems. On the other hand, asymmetric propagation and storage schemes can be achieved by employing two control fields with different detunings, intensities, or temporal modulations. Particularly when the FW and BW transmission windows are totally separated in frequency, a frequency-tunable bidirectional isolator can be realized. Beyond conventional nonreciprocal optics, the direction-dependent transmission and storage enabled by our dual-channel scheme may provide distinct information channels for photonic routing and selective manipulation, offering potential applications in programmable photonic quantum information processing.

A Derivation of the reduced Maxwell–Bloch equations

In the electric-dipole and rotating-wave approximations, the semiclassical interaction Hamiltonian in the interaction picture is

$$\begin{aligned}\widehat{H}_I = -\hbar\Big[&\Omega_{\mathrm{c}+}e^{-i\Delta_{\mathrm{c}+}t+ik_{\mathrm{c}+}z}|4\rangle\langle 2| + \Omega_{\mathrm{d}-}e^{-i\Delta_{\mathrm{d}-}t-ik_{\mathrm{d}-}z}|4\rangle\langle 3| \\ &+ \big(\Omega_{\mathrm{p}+}e^{-i\Delta_{\mathrm{p}+}t+ik_{\mathrm{p}+}z} + \Omega_{\mathrm{p}-}e^{-i\Delta_{\mathrm{p}-}t-ik_{\mathrm{p}-}z}\big)|4\rangle\langle 1| + \mathrm{H.c.}\Big].\end{aligned} \tag{A1}$$

Here, $\Omega_{\mathrm{c}+}$, $\Omega_{\mathrm{d}-}$, and $\Omega_{\mathrm{p}\pm}$ are the half Rabi frequencies, and $\Delta_{\mathrm{c}+}$, $\Delta_{\mathrm{d}-}$, and $\Delta_{\mathrm{p}\pm}$ are the corresponding field detunings, as defined in the main text. The atomic density operator obeys the optical Bloch master equation

$$\dot{\rho} = -\frac{i}{\hbar}[\widehat{H}_I, \rho] + \mathcal{L}_\gamma[\rho], \tag{A2}$$

where $\mathcal{L}_\gamma$ describes relaxation and dephasing. For $(\alpha,\beta) = (2,1),(3,1),(4,1)$, its matrix elements are $\langle\alpha|\mathcal{L}_\gamma[\rho]|\beta\rangle = -\gamma_{\alpha\beta}\sigma_{\alpha\beta}$, where $\gamma_{\alpha\beta}$ is the decay rate of the coherence $\sigma_{\alpha\beta}$. For the 21, 31, and 41 matrix elements, Eq. (A2) takes the form

$$\begin{aligned}\dot{\sigma}_{21} =& -\gamma_{21}\sigma_{21} + i\Omega_{\mathrm{c}+}^{*}e^{i\Delta_{\mathrm{c}+}t-ik_{\mathrm{c}+}z}\sigma_{41} \\ &- i\big(\Omega_{\mathrm{p}+}e^{-i\Delta_{\mathrm{p}+}t+ik_{\mathrm{p}+}z} + \Omega_{\mathrm{p}-}e^{-i\Delta_{\mathrm{p}-}t-ik_{\mathrm{p}-}z}\big)\sigma_{24}, \\ \dot{\sigma}_{31} =& -\gamma_{31}\sigma_{31} + i\Omega_{\mathrm{d}-}^{*}e^{i\Delta_{\mathrm{d}-}t+ik_{\mathrm{d}-}z}\sigma_{41} \\ &- i\big(\Omega_{\mathrm{p}+}e^{-i\Delta_{\mathrm{p}+}t+ik_{\mathrm{p}+}z} + \Omega_{\mathrm{p}-}e^{-i\Delta_{\mathrm{p}-}t-ik_{\mathrm{p}-}z}\big)\sigma_{34}, \\ \dot{\sigma}_{41} =& -\gamma_{41}\sigma_{41} + i\Omega_{\mathrm{c}+}e^{-i\Delta_{\mathrm{c}+}t+ik_{\mathrm{c}+}z}\sigma_{21} + i\Omega_{\mathrm{d}-}e^{-i\Delta_{\mathrm{d}-}t-ik_{\mathrm{d}-}z}\sigma_{31} \\ &+ i\big(\Omega_{\mathrm{p}+}e^{-i\Delta_{\mathrm{p}+}t+ik_{\mathrm{p}+}z} + \Omega_{\mathrm{p}-}e^{-i\Delta_{\mathrm{p}-}t-ik_{\mathrm{p}-}z}\big)(\sigma_{11}-\sigma_{44}).\end{aligned} \tag{A3}$$

For weak probes, population transfer from the initial state $|1\rangle$ is negligible. To first order in the probe fields, we take $\sigma_{11} \simeq 1$, $\sigma_{22} \simeq \sigma_{33} \simeq \sigma_{44} \simeq 0$, and $\sigma_{24} \simeq \sigma_{34} \simeq 0$, while retaining σ_{21}, σ_{31}, and σ_{41}. Under these approximations, Eq. (A3) reduces to Eq. (4).

For moving atoms, Eq. (5) includes the Doppler shifts of the four fields. The optical coherence σ_{41} contains the two probe phase factors $e^{-i(\Delta_{\mathrm{p}\pm}\pm kv)t\pm ikz}$. In Eq. (5), σ_{41} drives σ_{21} and σ_{31} through the conjugate control-field phase factors $e^{i(\Delta_{\mathrm{c}+}+kv)t-ikz}$ and $e^{i(\Delta_{\mathrm{d}-}-kv)t+ikz}$, respectively. Multiplying the probe phase factors by these conjugate factors determines the phase factors of the spin coherences σ_{21} and σ_{31} in Eq. (6). The co-propagating pairs generate the zero-wave-vector components $\widetilde{\sigma}_{21}^{(0)}$ and $\widetilde{\sigma}_{31}^{(0)}$, while the counter-propagating pairs generate $\widetilde{\sigma}_{21}^{(-2)}$ and $\widetilde{\sigma}_{31}^{(+2)}$ with wave vectors $-2k$ and $+2k$, respectively.

In the standing-wave Λ scheme of Ref. [62], both control fields drive the same transition and couple successive spatial harmonics. Here, $\Omega_{\mathrm{c}+}$ and $\Omega_{\mathrm{d}-}$ drive $|2\rangle \leftrightarrow |4\rangle$ and $|3\rangle \leftrightarrow |4\rangle$, respectively. Thus, $\widetilde{\sigma}_{21}^{(0)}$ and $\widetilde{\sigma}_{31}^{(+2)}$ couple back only to $\widetilde{\sigma}_{41}^{(+1)}$, whereas $\widetilde{\sigma}_{21}^{(-2)}$ and $\widetilde{\sigma}_{31}^{(0)}$ couple back only to $\widetilde{\sigma}_{41}^{(-1)}$. For atoms initially in $|1\rangle$, no additional spatial harmonics are generated at first order in the probes, so the six components in Eq. (6) form a closed set. Equation (7) follows by substituting Eq. (6) into Eq. (5) and equating coefficients of the same phase factors.

Equation (7), together with the Maxwell equations (10) obtained in the slowly varying envelope approximation, describes the pulse dynamics. During storage and retrieval, the control fields vary slowly so that the system follows the EIT dark state adiabatically [63,64].

Data availability statement

Data underlying the results presented in this paper are not publicly available at this time but may be obtained from the authors upon reasonable request.

Acknowledgment

This work is supported by the Natural Science Foundation of China (Grant No. 12104107) and the Guangxi Young Elite Scientist Sponsorship Program (Grant No. GXYESS2025075).

References

[1] Maynard M A, Bretenaker F, and Goldfarb F 2014 *Phys. Rev. A* **90** 061801(R)
[2] Lauprêtre T, Kumar S, Berger P, Faoro R, Ghosh R, Bretenaker F, and Goldfarb F 2012 *Phys. Rev. A* **85**(5) 051805(R)
[3] Picque J L and Pinard J 1976 *J. Phys. B* **9** L77
[4] Rastogi A, Saglamyurek E, Hrushevskyi T, Hubele S, and LeBlanc L J 2019 *Phys. Rev. A* **100** 012314
[5] Lezama A, Barreiro S, and Akulshin A M 1999 *Phys. Rev. A* **59** 4732
[6] Fleischhauer M, Imamoglu A, and Marangos J P 2005 *Rev. Mod. Phys.* **77** 633
[7] Javan A, Kocharovskaya O, Lee H, and Scully M O 2002 *Phys. Rev. A* **66** 013805
[8] Iftiquar S M, Karve G R, and Natarajan V 2008 *Phys. Rev. A* **77** 063807
[9] Zhang S, Hu Y, Lin G, Niu Y, Xia K, Gong J, and Gong S 2018 *Nat. Photonics* **12** 744
[10] Jalas D, Petrov A, Eich M, Freude W, Fan S, Yu Z, Baets R, Popović M, Melloni A, Joannopoulos J D, Vanwolleghem M, Doerr C R, and Renner H 2013 *Nat. Photonics* **7** 579
[11] Yu Z and Fan S 2009 *Nat. Photonics* **3** 91
[12] Zhan Y, Zhang J, Zhang S, Gong S, and Niu Y 2025 *Opt. Express* **33** 4491
[13] Xu X W and Li Y 2015 *Phys. Rev. A* **91** 053854
[14] Xia K, Nori F, and Xiao M 2018 *Phys. Rev. Lett.* **121** 203602
[15] Li G, Xiao X, Li Y, and Wang X 2018 *Phys. Rev. A* **97** 023801
[16] Zhou J, Yin X L, and Liao J Q 2023 *Phys. Rev. A* **107** 063703
[17] Abdo B, Sliwa K, Frunzio L, and Devoret M 2013 *Phys. Rev. X* **3** 031001
[18] Shen Z, Zhang Y L, Chen Y, Sun F W, Zou X B, Guo G C, Zou C L, and Dong C H 2018 *Nat. Commun.* **9** 1797
[19] Hu Y D, and Zhang G Q 2023 *Phys. Rev. A* **107** 053716
[20] Sounas D L, and Alù A 2017 *Nat. Photonics* **11** 774
[21] Lira H, Yu Z, Fan S, and Lipson M 2012 *Phys. Rev. Lett.* **109** 033901
[22] Estep N A, Sounas D L, Soric J, and Alù A 2014 *Nat. Phys.* **10** 923
[23] Wang J, Shi Y, and Fan S 2020 *Opt. Express* **28** 11974
[24] Peng B, Özdemir S K, Lei F , Monifi F, Gianfreda M, Long G L, Fan S, Nori F, Bender C M, and Yang L 2014 *Nat. Phys.* **10** 394
[25] Chang L, Jiang X, Hua S, Yang C, Wen J, Jiang L, Wang G, Li G, and Xiao M 2014 *Nat. Photonics* **8** 524
[26] Del Bino L, Silver J M, Woodley M T M, Stebbings S L, Zhao X, and Del' Haye P 2018 *Optica* **5** 279
[27] Fang K, Luo J, Metelmann A, Matheny M H, Marquardt F, Clerk A A, and Painter O 2017 *Nat. Phys.* **13** 465
[28] Hafezi M, and Rabl P 2012 *Opt. Express* **20** 7672

[29] Shen Z, Zhang Y L, Chen Y, Zou C L, Xiao Y F, Zou X B, Sun F W, Guo G C, and Dong C H 2016 *Nat. Photonics* **10** 657

[30] Ruesink F, Miri M A, Alù A, and Verhagen E 2016 *Nat. Commun.* **7** 13662

[31] Xu H, Jiang L, Clerk A A, and Harris J G 2019 *Nature* **568** 65

[32] Chen Y T, Du L, Liu Y M, and Zhang Y 2020 *Opt. Express* **28** 7095

[33] Kongkui Berinyuy E, Peng J X, Djorwé P, Abdourahimi, Abdel-Aty A H, Nisar K S, and Engo S N 2025 *Quantum Inf. Process.* **24**(6) 160

[34] Lodahl P, Mahmoodian S, Stobbe S, Rauschenbeutel A, Schneeweiss P, Volz J, Pichler H, and Zoller P 2017 *Nature* **541** 473

[35] Xia K, Lu G, Lin G, Cheng Y, Niu Y, Gong S, and Twamley J 2014 *Phys. Rev. A* **90** 043802

[36] Sayrin C, Junge C, Mitsch R, Albrecht B, O'Shea D, Schneeweiss P, Volz J, and Rauschenbeutel A 2015 *Phys. Rev. X* **5**(4) 041036

[37] Scheucher M, Hilico A, Will E, Volz J, and Rauschenbeutel A 2016 *Science* **354** 1577

[38] Chen Y T, Du L, Guo L, Wang Z, Zhang Y, Li Y, and Wu J H 2022 *Commun. Phys.* **5** 215

[39] Horsley S A R, Wu J H, Artoni M, and La Rocca G C 2013 *Phys. Rev. Lett.* **110** 223602

[40] Ramezani H, Jha P K, Wang Y, and Zhang X 2018 *Phys. Rev. Lett.* **120** 043901

[41] Yang L, Zhang Y, Yan X B, Sheng Y, Cui C L, and Wu J H 2015 *Phys. Rev. A* **92** 053859

[42] Wang D W, Zhou H T, Guo M J, Zhang J X, Evers J, and Zhu S Y 2013 *Phys. Rev. Lett.* **110** 093901

[43] Lin G, Zhang S, Hu Y, Niu Y, Gong J, and Gong S 2019 *Phys. Rev. Lett.* **123** 033902

[44] Fan S, Qi Y, Lin G, Niu Y, and Gong S 2020 *Opt. Commun.* **462** 125343

[45] Fan S, Qi Y, Niu Y, and Gong S 2022 *Chin. Opt. Lett.* **20** 012701

[46] Dong M X, Xia K Y, Zhang W H, Yu Y C, Ye Y H, Li E Z, Zeng L, Ding D S, Shi B S, Guo G C and Nori F 2021 *Sci. Adv.* **7** eabe8924

[47] Zhang S, Lin G, Hu Y, Qi Y, Niu Y, and Gong S 2020 *Phys. Rev. Appl.* **14** 024032

[48] Hu Y, Liu L, Zhang S, Li X, Qian J, Lin G, Niu Y, and Gong S 2021 *Opt. Commun.* **489** 126861

[49] Zhao H M, Zheng D D, Zhang X J, and Wu J H 2024 *New J. Phys.* **26** 043018

[50] Hu Y, Zhang S, Qi Y, Lin G, Niu Y, and Gong S 2019 *Phys. Rev. Appl.* **12** 054004

[51] Hu Y, Zhang S, Kuang X, Qi Y, Lin G, Gong S, and Niu Y 2020 *Opt. Express* **28** 38710

[52] Song F, Wang Z, Li E, Yu B, and Huang Z 2022 *Phys. Rev. Appl.* **18** 024027

[53] Liang C, Liu B, Xu A N, Wen X, Lu C, Xia K, Khoon Tey M, Liu Y C, and You L 2020 *Phys. Rev. Lett.* **125** 123901

[54] Lu X D, Cao W X, Yi W, Shen H, and Xiao Y H 2021 *Phys. Rev. Lett.* **126** 223603

[55] Shui T, Yang W X, Cheng M T, and Lee R K 2022 *Opt. Express* **30** 6284

[56] Chen T Y, and Wu J H 2026 *Phys. Rev. Res.* **8** 023212

[57] Paspalakis E and Knight P L 2002 *J. Opt. B: Quantum Semiclass. Opt.* **4** S372

[58] Mazets I E 2005 *Phys. Rev. A* **71** 023806

[59] MacRae A, Campbell G, and Lvovsky A I 2008 *Opt. Lett.* **33** 2659

[60] Wang H, Li S, Xu Z X, Zhao X B, Zhang L J, Li J H, Wu Y L, Xie C D, Peng K C, and Xiao M 2011 *Phys. Rev. A* **83** 043815

[61] Ham B S and Hemmer P R 2000 *Phys. Rev. Lett.* **84** 4080

[62] Wu J H, Artoni M, and La Rocca G C 2010 *Phys. Rev. A* **82** 013807

[63] Phillips D F, Fleischhauer A, Mair A, Walsworth R L, and Lukin M D 2001 *Phys. Rev. Lett.* **86** 783

[64] Kuklinski J R, Gaubatz U, Hioe F T, and Bergmann K 1989 *Phys. Rev. A* **40** 6741